Volumetric Attribute Filtering and Interactive Visualization Using the Max-Tree Representation

Michel A. Westenberg, Jos B. T. M. Roerdink, *Senior Member, IEEE*, and Michael H. F. Wilkinson, *Senior Member, IEEE*

***Abstract*—The Max-Tree designed for morphological attribute filtering in image processing, is a data structure in which the nodes represent connected components for all threshold levels in a data set. Attribute filters compute some attribute describing the shape or size of each connected component and then decide which components to keep or to discard. In this paper, we augment the basic Max-Tree data structure such that interactive volumetric filtering and visualization becomes possible. We introduce extensions that allow 1) direct, splatting-based, volume rendering; 2) representation of the Max-Tree on graphics hardware; and 3) fast active cell selection for isosurface generation. In all three cases, we can use the Max-Tree representation for visualization directly, without needing to reconstruct the volumetric data explicitly. We show that both filtering and visualization can be performed at interactive frame rates, ranging between 2.4 and 32 frames per seconds. In contrast, a standard texture-based volume visualization method manages only between 0.5 and 1.8 frames per second. For isovalue browsing, the experimental results show that the performance is comparable to the performance of an interval tree, where our method has the advantage that both filter threshold browsing and isolevel browsing are fast. It is shown that the methods using graphics hardware can be extended to other connected filters.**

***Index Terms*—Connected filters, mathematical morphology, Max-Tree, nonlinear filtering, volume visualization.**

I. Introduction

ATTRIBUTE filters are a subset of morphological connected filters, a class of shape-preserving filters used in image processing [1]–[8]. Examples of such filters are area openings and closings, which remove image detail smaller than a particular area [9]. More general are the attribute openings, which accept or reject image details based on size criteria [10]. Similarly, it is also possible to filter on shape, rather than on size criteria. This idea has been formalized as so-called shape filters [11], [12], which have been extended to 3-D and have been applied to the problem of vessel enhancement in angiographic volume data sets [13].

These filters are different from the morphological erosion- and dilation-based operations in that they do not make use of structuring elements, but rather retain or discard connected components as a whole. An example of an attribute filter applied to a grey scale volume is shown in Fig. 1. The left image shows an isosurface visualization of the original data, and the right image shows an isosurface visualization of the result of filtering the data with an attribute filter that is selective for noncompact structures [13]. For both images, the same isovalue $t = 13$ was used. A computationally efficient implementation of these filters is based on a data structure called the Max-Tree [14].

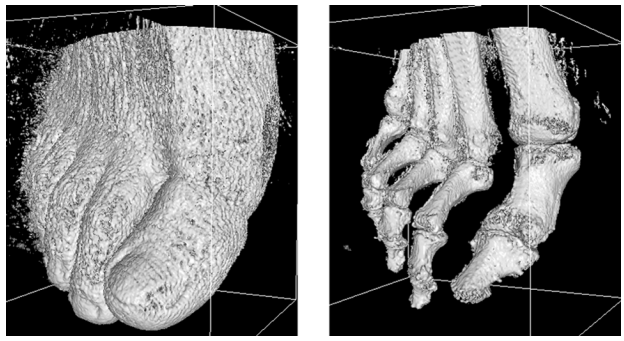

Fig. 1. Attribute filtering of a volume with a filter that selects noncompact structures: (left) original data; (right) filtered data. Rendering is done with an isosurface, and for both images, an isolevel threshold $t = 13$ was used.

In previous work, we have developed a volumetric filtering method based on attribute filters, and we have combined it with a basic volume visualization method [15]. In that work, we have shown that filtering can be done at interactive rates; however, this was not the case for visualization. The reason is that we first reconstructed the filtered volume data, and then applied a visualization method. The purpose of this paper is to extend the Max-Tree data structure, such that filtering *and* visualization can be done directly from this extended Max-Tree. We will show that this can be done at interactive rates. Since there is often no *a priori* "right" filter threshold, such interactive feedback is essential. As visualization methods, we employ both direct volume rendering and isosurface rendering. The direct volume rendering approaches most useful for our application are splatting [16] and 3-D hardware texture mapping [17]. For isosurface visualization, the extensions proposed in this paper allow fast selection of cells that intersect the isosurface (active cells) when varying the attribute filter threshold and also when varying the isovalue threshold.

The organization of the paper is as follows. Section II describes previous work on attribute filters, the Max-Tree data structure, and volume-rendering methods. We introduce three new attributes in Section III. In Section IV, we introduce the augmented Max-Tree and the visualization methods that make use of the augmented data structure. We compare the results of our new method with that of some standard approaches in Section V. Finally, Section VI discusses the results and possible future extensions.

Manuscript received January 16, 2007; revised August 6, 2007. The associate editor coordinating the review of this manuscript and approving it for publication was Prof. Philippe Salembier.

The authors are with the Institute of Mathematics and Computing Science, University of Groningen, Groningen, The Netherlands (e-mail: m.a.westenberg@rug.nl; j.b.t.m.roerdink@rug.nl; m.h.f.wilkinson@rug.nl).

Digital Object Identifier 10.1109/TIP.2007.909317

II. Previous Work

A. Attribute Filters and the Max-Tree

An efficient implementation of attribute filters relies on computing both the hierarchy of connected components in the data set and some attribute for each component. The Max-Tree was introduced to separate the computation of these from the actual filtering process [14].

Max-Trees are closely related to contour trees [18]–[21]. In particular, the join trees used to compute contour trees are essentially the same as Max-Trees, especially when they are augmented to include attribute information in each node [22]. A key difference between the Max-Tree and the join tree is that, in the latter case, it is usually assumed that all nodes in the grid of data have a unique (grey) value. By contrast, Max-Trees were designed to administrate flat zones, i.e., connected sets of vertices with the same grey value. Contour trees themselves are equivalent to *level-line trees* [23], which can be constructed from a Max-tree and a Min-Tree of the same image.

1) Construction: Let $\mathbf{M} \subseteq \mathbb{R}^3$ be the volume domain, and $f : \mathbf{M} \rightarrow \mathbb{R}$ the grey scale volume. We implicitly assume the existence of a grid on $\mathbf{M}$, and we use a 26-connected voxel neighborhood.

A Max-Tree is a tree where the nodes represent sets of *flat zones* of f. A set $F \subset \mathbf{M}$ is called a flat zone if for all $p, q \in F$ there exists a path from p to q along which the function value is constant, and the set F is maximal in size. The threshold set $X_h(f)$ of f is the set of points that remain after thresholding at level h, i.e.,

$$X_h(f) = \{x \in \mathbf{M} | f(x) \geq h\}. \tag{1}$$

A *peak component* P_h^k at a grey level h can then be defined as the kth connected component of the threshold set $X_h(f)$. A Max-Tree node C_h^k represents one or more flat zones at grey level h contained in a single peak component at the same level. A simple 1-D example for a signal with nine elements is shown in Fig. 2(a). The signal also has nine flat zones, since none of the signal elements is connected to another element of the same value. The values range between zero and three; therefore, there are four threshold sets, of which only $X_2(f)$ contains two connected components.

The Max-Tree can be constructed by a recursive flooding procedure that makes use of a hierarchical FIFO queue to process the voxels in correct order [14] or by relying on Tarjan's union-find algorithm [24], [25]. In this paper, we use the queue-based approach.

2) Filtering: Filtering removes Max-Tree nodes based on some property defined by an attribute value $A(P_h^k)$ of a node C_h^k, from a universe (typically, $\mathbb{R}$ or $\mathbb{Z}$) on which an order $\leq$ exists. Given a threshold value λ from this universe, the algorithm decides whether to preserve, or remove a node. Two classes of strategies exist 1) *pruning strategies*, which remove all descendants of C_h^k, if C_h^k is removed; and 2) *nonpruning strategies*, in which the parent pointers of children of C_h^k are updated to point at the oldest "surviving" ancestor of C_h^k.

Salembier describes four different rules for the algorithm to filter the tree: the *Min*, the *Max*, the *Viterbi*, and the *Direct* decision. The first three are pruning strategies. In addition, Wilkinson and Urbach [11] introduced another nonpruning strategy, called the *Subtractive* decision. The decisions of these rules are as follows.

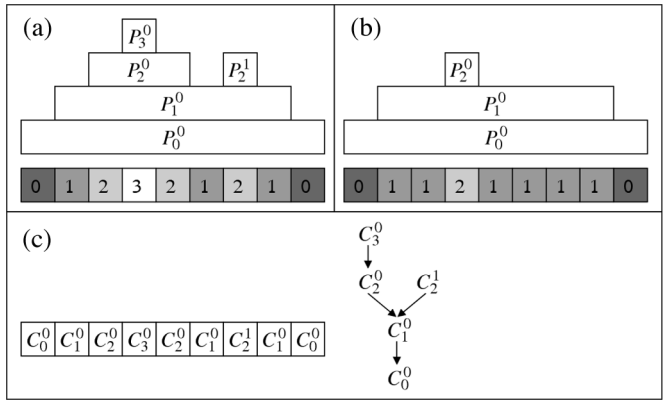

Fig. 2. (a) Input 1-D signal and corresponding peak components. (b) Signal and corresponding peak components after filtering in the case that the attribute values $A(P_2^0)$ and $A(P_2^1)$ do not satisfy the filter criterion. (c) Max-Tree of the input signal and mapping between signal elements and Max-Tree nodes.

Min	A node C_h^k is removed if $A(P_h^k) < \lambda$ or if one of its ancestors is removed.
Max	A node C_h^k is removed if $A(P_h^k) < \lambda$ and all of its descendant nodes are removed, as well.
Viterbi	The removal and preservation of nodes is considered as an optimization problem. For each leaf node, the path with the lowest cost to the root node is taken, where a cost is assigned to each transition. In this paper, we do not consider this rule. For details see Salembier *et al.* [14].
Direct	A node C_h^k is removed if $A(P_h^k) < \lambda$; its pixels are lowered in grey level to the highest ancestor which meets the criterion, its descendants are unaffected.
Subtractive	As above, but the descendants are lowered by the same amount as C_h^k itself.

Fig. 2(b) shows the results of filtering the signal in Fig. 2(a) using the subtractive decision rule.

3) Restitution: In a single pass through the destination volume, each voxel is assigned the new grey level of the corresponding node in the Max-Tree. It is this phase that we skip and replace by a visualization phase in this work.

B. Volume Rendering

Volume rendering is the process of generating 2-D images from 3-D data. It is pervasive in many application areas, such as medical imaging, biology, and computational fluid dynamics. Basically, two approaches exist: surface fitting methods and direct volume rendering methods [26].

Surface fitting methods extract constant-value surfaces representing the boundary between materials. By taking different threshold values, distinct isosurfaces can be extracted from the

volume data by fitting geometric primitives such as triangle meshes to the boundaries that match the threshold [27].

Direct volume rendering methods [28] do not make use of intermediate graphical primitives, but make a direct mapping from the volume data onto the view plane. A standard method, called *X-ray rendering*, is to integrate the data values along the line of sight. *Maximum intensity projection* (MIP) takes the maximum value encountered along this line. This method is used often to visualize magnetic resonance angiography (MRA) data. Most other methods require a classification step, in which colors and opacities are assigned to ranges of data values. The opacities are used to make some parts transparent in order to reveal the interesting parts.

Much effort has been spent on speeding up the fundamental volume rendering techniques, see [29] for an overview. For isosurface visualization, an expensive step is to select the active cells, i.e., those cells that intersect the isosurface. There are two basic approaches: range-based search methods and seed set generation methods. The range-based methods use an interval $[a, b]$ of the range of the scalar field values of a cell, where a is its minimum value and b its maximum. Given an isovalue threshold t, a cell is intersected by the isosurface if $a \leq t \leq b$. A popular range-based method is the interval tree [30], which is a balanced binary search tree that stores the intervals, and which can be queried efficiently. The seed set generation methods construct a small group of cells, the seed set, which includes at least one active cell for each possible isosurface. Starting from the seed set, adjacent isosurface cells are found by propagation methods [20], [31], [32].

Acceleration techniques for direct volume rendering often involve ways to skip empty space, for example, by storing the data in an octree [33]. There also exist transform domain approaches, based on a wavelet decomposition of the data [34], [35] or a Fourier representation [36], [37]. The best rendering speed is currently provided by specialized hardware, such as VolumePro [38], or texture mapping on standard PC graphics cards [17], [39].

Practically all acceleration methods have one problem in common: the underlying data structures cannot be updated easily if the volume data change as a result of, for instance, filtering. In general, the data structure has to be completely rebuilt, imposing large delays between filtering and rendering. The standard hardware-based texture mapping approach is also not directly usable, since the whole volume has to be transferred from main memory to graphics card memory, a step which is expensive. In the next section, we will introduce extensions to the basic Max-Tree that will allow us to visualize the data directly from the Max-Tree representation.

III. Attributes

Any attribute of a connected component can be used with the Max-Tree. If it is required that the Max-Tree building phase is short, it should be possible to compute the attribute incrementally. An example is the volume of a connected component, which can easily be updated voxel by voxel. Other examples are the length of the diagonal of the bounding box or the minimum enclosing box; the radius, diameter, or volume of the smallest enclosing sphere; the moment of inertia; the perimeter, or criteria derived from the perimeter, such as complexity, simplicity, compactness, eccentricity, jaggedness, etc. [10], [14]. However, if the Max-Tree building process can be done off-line, this restriction does not hold, and any shape or size attribute can be used. Examples are radius of the largest inscribed circle, skeleton length, etc.

Previously, Wilkinson and Westenberg [13] proposed a scale-invariant attribute based on the moment-of-inertia tensor of each object for vessel enhancement filtering. The moment-of-inertia tensor $\mathbf{I}(C)$ of an object C can be defined as

$$\mathbf{I}(C) = \begin{pmatrix} I_{xx}(C) & I_{xy}(C) & I_{xz}(C) \\ I_{xy}(C) & I_{yy}(C) & I_{yz}(C) \\ I_{xz}(C) & I_{yz}(C) & I_{zz}(C) \end{pmatrix} \tag{2}$$

with

$$I_{xx}(C) = \sum_C (x - \bar{x})^2 + V(C)/12 \tag{3}$$

$$I_{yy}(C) = \sum_C (y - \bar{y})^2 + V(C)/12 \tag{4}$$

$$I_{zz}(C) = \sum_C (z - \bar{z})^2 + V(C)/12 \tag{5}$$

$$I_{xy}(C) = \sum_C (x - \bar{x})(y - \bar{y}) \tag{6}$$

$$I_{xz}(C) = \sum_C (x - \bar{x})(z - \bar{z}) \tag{7}$$

and

$$I_{yz}(C) = \sum_C (y - \bar{y})(z - \bar{z}) \tag{8}$$

in which $V(C)$ stands for the volume of C, and $\bar{x}$, $\bar{y}$, and $\bar{z}$ denote the centre of mass coordinates. The term $V(C)/12$ in the diagonal terms corrects for the moment-of-inertia contribution of each of the individual voxels, which are considered to be small cubes. This correction is necessary for two reasons: 1) it ensures scale invariance more precisely, and 2) it prevents division-by-zero errors caused by zero eigenvalues. Tensor $\mathbf{I}$ is essentially the covariance matrix multiplied by the number of voxels in C. It can be computed for each node of the tree by computing $\sum x^2, \sum y^2, \sum z^2, \sum xy, \sum xz, \sum yz, \sum x, \sum y, \sum z$, and volume. Each of these is easily updated incrementally.

Several moment-invariants can be computed from the moment-of-inertia tensor. The noncompactness attribute $\mathcal{N}(C)$ used for vessel enhancement [13] is defined as

$$\mathcal{N}(C) = \frac{\mathrm{Tr}\mathbf{I}(C)}{V^{5/3}(C)}. \tag{9}$$

It can be shown that this is a 3-D counterpart of the first moment invariant of Hu [40], and it was previously proposed outside the filtering context in [41]. Other 3-D moment invariants are discussed in [42]. Here, we derive other moment-invariants which have a straightforward geometric interpretation from the eigenvalues of $\mathbf{I}$. Let $\lambda_1(C)$, $\lambda_2(C)$, and $\lambda_3(C)$ be the three (real) eigenvalues of $\mathbf{I}(C)$, sorted such that

$$|\lambda_1(C)| \geq |\lambda_2(C)| \geq |\lambda_3(C)|. \tag{10}$$

Intuitively, $\lambda_1(C)$ is the variance along the major axis, multiplied by the volume of the object, and likewise for the other two eigenvalues. Therefore, the ratios

$$\mathcal{E}(C) = \left| \frac{\lambda_1(C)}{\lambda_2(C)} \right| \tag{11}$$

and

$$\mathcal{F}(C) = \left| \frac{\lambda_2(C)}{\lambda_3(C)} \right| \tag{12}$$

are measures of *elongation* and *flatness*, respectively. Furthermore, the lengths $d_i(C)$ of the principal axes can be estimated as

$$d_i(C) = \sqrt{\frac{20\,|\lambda_i(C)|}{V}}. \tag{13}$$

Finally, the *sparseness* $\mathcal{S}$ can be computed as

$$\mathcal{S}(C) = \frac{\pi d_1 d_2 d_3}{6\,\mathrm{V}} \tag{14}$$

i.e., it is the ratio of the volume expected given its principal axes, over the actual volume. It attains a minimum of 1 for solid spheres and ellipsoids, is equal to about 1.127 for solid rectangular blocks, and becomes higher as the object becomes either hollowed out or tree-like.

IV. Augmented Max-Tree

In the usual implementation of the filtering phase, the Max-Tree structure is modified by removing nodes from the tree. In order to be able to reuse the same Max-Tree for filtering with different values for the threshold parameter λ, nodes should not actually be removed from the tree. Therefore, we explicitly store the grey value of a node C_h^k in an extra field. We introduce the notation $g(C_h^k)$ to denote this *current* grey value. The current grey value is initialized as $g(C_h^k) = h$, i.e., the original grey value of the node, and it is updated during filtering. The filtering phase now uses the original grey value of a node C_h^k, and stores the grey value resulting after filtering as $g(C_h^k)$.

We will replace the restitution phase, since reconstructing the complete volume is not convenient for visualization purposes. Instead, we introduce a few extensions that allow us to use the Max-Tree representation directly for visualization.

A. Splatting

Splatting is a visualization method that traverses the voxels and calculates the projection and contribution of a voxel to the pixels in the view plane [16]. In the method, the underlying continuous function is reconstructed from the discrete volume data by convolution with a reconstruction filter, followed by a mapping to the view plane by superposition of building blocks called *footprints*. The footprints are the result of integrating the reconstruction kernels along the line of sight. For orthographic projection, the footprints are the same for all voxels, and have to be computed only once for a given viewing direction.

MIP and X-ray rendering can be implemented very efficiently [35], [43], since the voxels can be processed in arbitrary order. Though it is possible to perform semi-transparent rendering by depth sorting the voxels, we restrict our splatting implementation to MIP and X-ray rendering, since splatting is to be used as a previewing method. A more sophisticated rendering algorithm is presented in Section IV-B.

Before we can describe the rendering algorithm, it is necessary to establish a mapping from Max-Tree nodes to voxels. During the construction phase, we fill a list L with voxel coordinates in a lexicographical order according to grey value and Max-Tree node index. In each Max-Tree node, two extra fields are maintained: an offset in the list L, and the number of voxels that belong to that node. In essence, the list L is just a flattened representation of the hierarchical queues, which are used in the flooding procedure.

The rendering algorithm starts at the root node, and traverses the tree to the leaves. At each node C_h^k, the current grey value $g(C_h^k)$ is inspected, and if $g(C_h^k) > 0$ (the background color), the voxels belonging to the node are looked up in the list L. For all voxels, we calculate the projection p of the center of each voxel v on the view plane. For MIP, v only contributes to the pixel closest to p. For X-ray rendering, we distribute the contribution linearly to the four pixels closest to p. The final step is to close holes that appear for nonaxial views. For X-ray rendering, this is done by convolving the image with the splatting footprint [35]. Since linear interpolation does not combine very well with MIP [44], we use morphological sampling [45], and it has been shown that the footprints from classical splatting have to be replaced by a morphological closing in the view plane [43].

B. Hardware-Assisted Volume Rendering

Modern graphics cards support 2-D or 3-D texture mapping functionality, which can be used to implement volume rendering based on texture slicing [17], [39].

Volume rendering by 3-D texture mapping works as follows. The volume data are loaded as a 3-D texture T in texture memory on the graphics hardware. Modern cards usually have 256-MB or 512-MB memory available. Next, polygons parallel to and at increasing distances from the view plane are generated. Resampling is then performed at the intersections of these polygons and T, a process during which trilinear interpolation is used. The resulting scalar values are then mapped to color and opacity by a transfer function that is also stored on the hardware as a 1-D texture. This is called a dependent texture lookup: the interpolated scalar value is used as an index in the transfer function texture. Finally, the polygons are blended in a back-to-front order to make the final image. The whole process takes place in hardware, and it can be implemented in a straightforward way in OpenGL and a so-called fragment program. A fragment is simply a pixel with associated color and depth value. In OpenGL, it is possible to replace the standard fragment operations, such as texture mapping, color operations, fog calculations, for example, by a fragment program that performs some other operation.

A bottleneck in the approach above is volume reconstruction from the Max-Tree and transfer of the volume data from main memory to the graphics card. For a moderately-sized data set of 256^3 voxels, this can take in the order of 500 to 5000 ms, depending on the hardware and the size of the Max-Tree. This

is more than one order of magnitude slower than the Max-Tree filtering phase (see also Section V). We, therefore, propose a slightly different approach.

We construct a 1-D array A, in main memory, containing all Max-Tree nodes with no specific ordering. Then, we make a volume data set T_v that for each voxel contains the index of the corresponding Max-Tree node in the array A, rather than the node's grey value. The volume T_v is transferred once to the graphics hardware. From the array A, we derive a 1-D texture T that contains the current grey values of the Max-Tree nodes. This texture is updated and transferred to the graphics hardware each time filtering is applied (see *Update* in Alg. 1). Transferring T will be much faster than transferring the whole volume data set, since in general the size of T is much smaller than the number of voxels. The rendering phase now requires one extra dependent texture lookup to obtain the grey value at a specific point when resampling T_v. Sampling a voxel v of T_v yields an index, which is used to find the grey value of v in T. A second dependent texture lookup occurs during the application of the transfer function, see *Draw* in Alg. 1.

Algorithm 1 Pseudo code for texture-based volume rendering

Update()

// $g(p)$ denotes current grey value of node p

for $i \leftarrow 0$ to length (A) **do**

$T[i] \leftarrow g(A[i])$

end for

Transfer T to graphics hardware

Draw()

for all slice planes s **do**

for all fragments f in s **do**

$i \leftarrow$ sample T_v in point f // Fetch node index

$g \leftarrow T[i]$ // Fetch current grey value

$f.\text{color} \rightarrow \text{TransferFunction}(g)$

end for

Blend s with frame buffer

end for

Due to limitations of the hardware, the actual implementation is somewhat more involved than sketched above. The first restriction is that textures can only have dimensions that are powers of two. Secondly, it is not possible to store integer-valued volume data directly, since the hardware only supports RGBA (red, green, blue, and alpha) components with eight bits per component. Furthermore, the size of a 1-D texture is usually also limited to about 4096. Therefore, we factorize the integer indices into RGB triplets: T_v becomes a 3-D RGB texture and T is turned into a 3-D texture. For example, consider a Max-Tree that contains 38868 nodes. Then, T will have dimensions $256 \times 256 \times 1$, and the node with integer index 2698 is factorized as $(R, G, B) = (10, 138, 0)$. This way of storing Max-Tree node indices limits the maximum number of nodes to 256^3. We cannot use the alpha component, since 4-D textures are not supported.

During resampling, we have to take care that T_v contains indices, so that trilinear interpolation cannot be used directly. This problem is solved by a fragment program which performs the interpolation. The input to the fragment program is the 3-D coordinate of the sample point p at which we need the grey value. The first step is to determine the coordinates of the eight voxels in T_v closest to p by simple rounding operations. This yields the indices to be used to access T to obtain the current grey values of these voxels. These grey values are then trilinearly interpolated to obtain the grey value at p. Finally, the transfer function is applied.

Since trilinear interpolation requires eight dependent texture lookups, it is computationally expensive. Therefore, we have also implemented a fragment program that performs nearest neighbor interpolation, i.e., it just finds the grey value of the voxel v closest to p. This requires only one dependent texture lookup, at the cost of reduced image quality.

C. Isosurfacing

To extract an isosurface efficiently from the Max-Tree representation, we need a few more extensions, which we introduce below. First, consider the following observations.

Let a cell c be identified by the corner voxel with the minimum coordinate values within the cell. Define the root path of a node C_h^k as the path through the tree that starts in C_h^k and ends in the root node, and which contains all nodes encountered on the descent. In case of a 26-connected neighborhood, two important properties hold: 1) all eight corner voxels of any given cell c are part of the same root path in the Max-Tree, since they are all neighbors of each other; 2) filtering in the Max-Tree does not change the grey-level order of Max-Tree nodes along a root path. To see that the first property holds, consider the following cases for two arbitrary voxels p and q of a cell c. If they have the same grey value, i.e., $f(p) = f(q)$, they belong to the same flat zone and, thus, the same Max-Tree node $C_{f(p)}^k$. If $f(p) < f(q)$, both voxels belong to the same connected component in the threshold set $X_{f(p)}$, and q is part of a flat zone of a child node of the Max-Tree node $C_{f(p)}^k$. In case $f(p) > f(q)$, the parent-child relation of p and q is inverted. The fact that the second property holds follows directly from the filtering rules discussed in Section II. Because of these properties, just *one* Max-Tree node $C_{h_1}^k$ defines a cell's minimum value and just *one* other Max-Tree node $C_{h_2}^m$ its maximum value. It is important to realize that, after filtering, the *same* nodes still define the cell's minimum and maximum value, even though the actual grey values of the nodes themselves may have changed.

We construct two label volumes, $V_{\min}$ and $V_{\max}$, which store for each cell c the Max-Tree node containing its minimal and maximal neighboring node, respectively. Note that, if the original volume has size $N_1 \times N_2 \times N_3$, there are $(N_1 - 1) \times (N_2 - 1) \times (N_3 - 1)$ cells. Next, we define edge cells as those cells c for which $V_{\min}(c) \neq V_{\max}(c)$. These are the cells that possibly contain an isosurface.

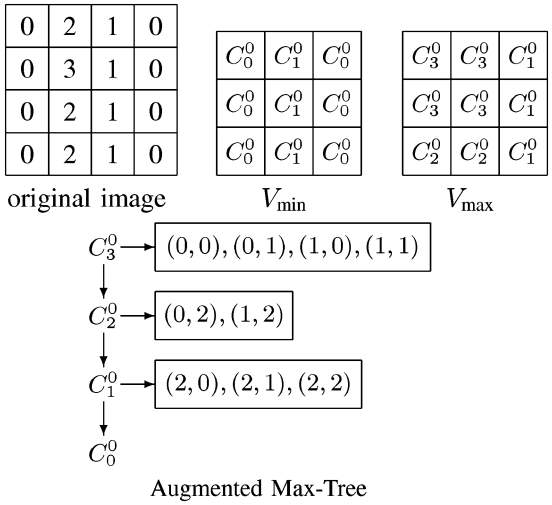

Fig. 3. Simple augmented Max-Tree. The top row shows a 4×4 image with 4 grey levels, and the (3×3) arrays containing $V_{\min}$ and $V_{\max}$, respectively. Below these, the augmented Max-Tree is shown, in which each node (except for the root) contains a pointer to an array of edge cell coordinates assigned to it (origin is upper left). Because there are four cells with $V_{\max} = C_3^0$ there are four cell coordinates in its edge cell array. Note that they are sorted in increasing order of the grey level of the corresponding node in $V_{\min}$.

The idea now is to store each edge cell c in the Max-tree node $V_{\max}(c)$. We store these edge cells in ascending order of the *current* grey value of their minimum neighboring Max-Tree node. Initially, the current grey level equals the original grey level $g(V_{\min}(c))$. Because all lower neighbors of a Max-tree node must belong to the same root path, and because the filtering retains the order of nodes in a root path, we may sort the edge cells assigned to each node in ascending order of $g(V_{\min}(c))$. Fig. 3 shows an example of the augmented Max-Tree for a simple 4×4 image.

The memory overhead of edge cell administration is $O(M + N)$, where M denotes the number of Max-Tree nodes and N the total number of cells. Assuming that s denotes the number of bytes required to store an integer or a pointer to a Max-Tree node, the exact memory overhead is $s(M + 2N)$ bytes: $V_{\min}$ contains N pointers to Max-Tree nodes, and each Max-Tree node contains an array of indices of edge cells and the size of this array. Note that M is usually much smaller than the number of voxels, but these numbers can become equal in the worst case.

Given an isolevel query value t, it is now straightforward to select the cells for which maximum and minimum grey values straddle this threshold (*active* cells). Because the leaves of the Max-Tree contain regional maxima, it is possible to descend from each leaf for which the current grey level is higher than t. At each node p that is visited, the algorithm checks whether it has not yet been processed and whether the current grey level $g(p) \geq t$. If so, the edge cells c_i^p of p are processed in ascending order, while the minimum *filtered* grey level of its minimum $f(V_{\min}(c_i^p)) \leq t$. When ready, the node is marked as processed, and the algorithm descends to the parent, until the root node is reached. The pseudo code for active cell selection is shown in Algorithm 2.

Algorithm 2 Pseudo code for active cell selection

// Isolevel query value is t; $g(p)$ denotes current grey value of node p.

for all nodes p **do**

    p.processed $\leftarrow$ false

end for

root.processed $\leftarrow$ true

for all leaves q **do**

    $p \leftarrow q$

    while (not p.processed) and $(g(p) \geq t)$ **do**

        $i \leftarrow 0$

        while $(i < p.\text{numEdges})$ and $(g(V_{\min}(c_i^p)) \leq t)$ **do**

            add c_i^p to active cell list

            $i \leftarrow i + 1$

        end while

        p.processed $\leftarrow$ true

        $p \leftarrow p$.parent

    end while

end for

The final step is to process the active cell list, and perform triangulation within each cell. This is done by analyzing the marching cubes cases [27], and constructing a triangulation accordingly. The normals of the corner voxels of the cell are re-computed each time the isolevel t or filter threshold λ changes. The triangulated isosurface is sent to the graphics hardware by means of OpenGL vertex arrays.

V. Results

To measure the performance of our method, we used two data sets available publicly from http://www.volvis.org and a third one from http://www9.informatik.uni-erlangen.de/External/vollib. The data sets are *foot* (courtesy Philips Research, Hamburg, Germany), a rotational b-plane X-ray scan; *aneurism*, a CT scan (courtesy Viatronix, Inc., USA); and *piggy bank*, also a CT scan (courtesy M. Bauer, Computer Graphics Group, University of Erlangen, Germany). Visualizations of these data sets are shown in Fig. 4, and the data set details are listed in Table I, including the Max-Tree construction time and the number of Max-Tree nodes. All timings were performed on a PC with 8 GB of memory, two dual core 2.4-GHz Opteron 280 CPUs, and two NVIDIA GeForce 7900 GTX graphics cards equipped with 512-MB memory each. Only one CPU and one graphics card were used for the timings.

We measured the computation time of the Volume attribute and the attributes defined in Section III. Table II lists the results. We did not include the timing results of the flatness (12) and

(a) (b) (c)

Fig. 4. (a) Isosurface visualization of the piggy bank data set. (b) MIP rendering of the foot data set. (c) MIP rendering of the aneurism data set, filtered by a criterion based on the noncompactness attribute (thresholded at $\lambda = 2.0$).

TABLE I
DATA SET DETAILS. THE SECOND AND THIRD COLUMN LIST THE NUMBER OF VOXELS AND THE DYNAMIC RANGE OF THE DATA. THE FOURTH AND FIFTH COLUMN LIST THE NUMBER OF MAX-TREE NODES AND THE MAX-TREE CONSTRUCTION TIME IN SECONDS

Name	Data set size	Dynamic range	Max-Tree nodes	M-T build time (s)
Piggy bank	11,796,480	12-bits	206,529	14.7
Foot	16,777,216	8-bits	279,513	16.4
Aneurism	66,846,720	8-bits	505,952	100.0

TABLE II
TIMINGS (IN MILLISECONDS) OF THE VOLUME, NONCOMPACTNESS, AND SPARSENESS ATTRIBUTES. ELONGATION AND FLATNESS ATTRIBUTES TAKE ABOUT THE SAME TIME AS THE SPARSENESS ATTRIBUTE AND HAVE NOT BEEN INCLUDED, THEREFORE

Data set	Volume	Non-compactness	Sparseness
Piggy bank	109	226	383
Foot	151	329	538
Aneurism	457	1,047	1,796

elongation (11) attributes, because they showed the same performance as the sparseness (14) attribute. This was expected, since the computation time in these three attributes is dominated by the eigenvalue calculation.

Fig. 5 contains timing results for browsing the filter threshold λ in the range [0, 25] for the elongation attribute (11), and subsequent direct volume rendering (MIP). All times are given in milliseconds. The plots compare splatting directly from the Max-Tree (Section IV-A) with our texture-based volume rendering approach (Section IV-B) for both nearest neighbor (MTNN) and trilinear interpolation (MTTL). We have also included a standard texture-based volume rendering approach in which the volume is reconstructed before it is sent to the graphics hardware (STBV). In all cases, the window size for displaying the final image was 400×400 pixels, and the number of slice planes for texture-based volume rendering was fixed to 300. Table III, in addition, lists the average times to perform filtering, transfers of data to the graphics hardware, and drawing time for the texture-based volume rendering methods. From the table, it is clear that filtering can be done at interactive rates. We must note here that the filtering time depends only on the number of Max-Tree nodes, and that it is independent of the choice of the filter criterion, which only affects the number of voxels in the filtered data set. Splatting and STBV are both highly dependent on the number of voxels that remain after filtering. Our approaches MTNN and MTTL show an almost constant behavior over the whole λ range. We can see that volume reconstruction and transfer in STBV is very costly, and that our method performs much better, because much less data has to be transferred.

In Table IV, we show the average frame rates (the number of times per second all data can be drawn to the screen) of all direct volume rendering methods. These rates were measured twice with over a full rotation around the z axis in increments of one degree. The first timing was performed with $\lambda = 0$ to measure performance on the raw data sets. For the second timing, we used a different criterion for each data set: for *foot*, the elongation attribute worked well on the bones, the flatness attribute revealed the coins in *piggy bank*, and the noncompactness attribute enhanced the vessels in *aneurism*. The threshold λ was set to a value that yielded a first interesting result, i.e., the moment components that do not satisfy the filtering criterion start to disappear. Splatting works only well for very low voxel counts. As expected, STBV is the fastest, because it requires only one dependent texture lookup during drawing. Our approach also shows high frame rates for nearest neighbor interpolation, and it is still quite fast for trilinear interpolation. During a rotation, or other user interaction such as zooming and panning, we, therefore, use nearest neighbor interpolation, and switch to trilinear interpolation when interaction ceases. Nearest neighbor interpolation has lower image quality (see Fig. 6), but it is acceptable during user interaction.

We also compared the performances of our isosurface extraction method and the interval tree. In the experiment, we increased the isovalue threshold t from the lowest data value to the maximum data value in steps of one or ten, depending on the dynamic range of the data. The performance measurement was carried out on the filtered data sets listed in Table IV. The interval tree had an overall somewhat better performance, which is not surprising, since it is optimized for the purpose of isovalue browsing. However, if we take interval tree construction time

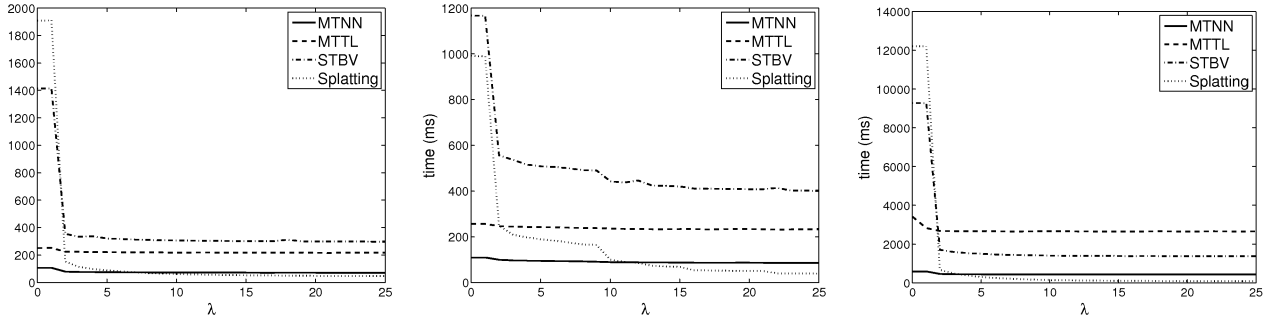

Fig. 5. Timing (ms) for browsing λ in the range [0, 25] for all datasets. Elongation (11) was used as a filter criterion. (a) Piggy bank; (b) foot; (c) aneurism.

TABLE III
AVERAGE TIMES (IN MILLISECONDS) FOR BROWSING THE FILTER THRESHOLD λ IN THE RANGE [0, 25]. THE SECOND COLUMN LISTS THE FILTERING TIME. THE THIRD COLUMN LISTS THE TIME TO TRANSFER THE LOOKUP TABLE T TO THE GRAPHICS HARDWARE, AND THE FOURTH AND FIFTH COLUMN SHOW THE DRAWING TIMES FOR MTNN AND MTTL, RESPECTIVELY. THE LAST TWO COLUMNS LIST THE TIME TO RECONSTRUCT AND TRANSFER THE FILTERED VOLUME DATA TO THE GRAPHICS HARDWARE AND THE DRAWING TIME FOR STBV, RESPECTIVELY

Data set	Filter	Max-Tree			STBV	
			MTNN	MTTL		
		transfer	draw	draw	transfer	draw
Piggy bank	20	40	20	149	367	12
Foot	27	51	19	143	465	12
Aneurism	33	92	276	2575	1985	17

TABLE IV
AVERAGE FRAME RATES MEASURED OVER A FULL ROTATION AROUND THE z AXIS. FOR EACH DATA SET, ANOTHER ATTRIBUTE WAS USED (SEE TEXT FOR DETAILS). WE FILTERED AT $\lambda = 0$ (RAW DATA) AND λ SET TO A VALUEFOR WHICH THE FIRST INTERESTING RESULT WAS OBTAINED

	Attribute	MTNN	MTTL	STBV	Splatting
Piggy bank	$\lambda = 0$	54.5	7.2	86.1	0.5
Foot	$\lambda = 0$	44.4	7.1	91.4	1.0
Aneurism	$\lambda = 0$	4.1	0.5	63.4	0.1
Piggy bank	$\lambda_F = 2.0$	56.5	7.2	94.2	8.6
Foot	$\lambda_E = 1.5$	57.4	7.3	93.0	5.5
Aneurism	$\lambda_{NC} = 2.0$	3.9	0.5	67.5	1.5

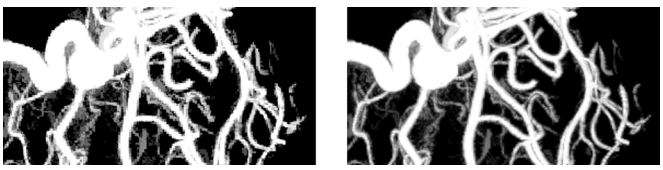

Fig. 6. Comparison between (left) nearest neighbor interpolation and (right) trilinear interpolation.

into account, which ranges between 0.9 and 56.0 s for our data sets, our approach that extracts an isosurface directly from the Max-Tree is more suitable when a user wants to perform both isovalue browsing and λ browsing.

Fig. 7 illustrates the effect of applying various attributes to the piggy bank data set. We used isosurfaces to visualize the results. The coins inside the piggy bank, which, incidentally, are made of chocolate in order to prevent scattering artifacts from the CT scanner, can be separated well by using the flatness attribute and a high threshold ($\lambda = 100.0$), see Fig. 7(a). The piggy bank is standing on a wooden block, see Fig. 7(b). The wood structure is well preserved by the sparseness attribute and a threshold of $\lambda = 6.5$. There is a hole in the piggy bank's belly, covered by a lid containing two springs that keep it in place. By filtering away nonelongated structures, these springs can be separated out (see Fig. 7). The elongation attribute was used with a threshold of $\lambda = 5.0$. Since our approach enables changing of attributes and thresholds at interactive rates, the images in Fig. 7 could be made within a few minutes. It would have been difficult and time consuming to achieve the same results without the visualization methods proposed in this paper.

We would like to refer the reader to our web page (http://www.rug.nl/informatica/onderzoek/programmas/svcg/demos), which contains a number of movies and a demo program. These demonstrate the interactivity offered by our method well.

VI. DISCUSSION

In this paper, we have proposed methods for interactive filtering and visualization of volume data sets based on a class of shape preserving filters. We have briefly reviewed such filters and explained how they can be implemented efficiently using Max-Trees, and we have also introduced new attributes based on 3-D moment invariants similar to those in [41] and [42]. The Max-Tree approach splits the filtering task in three stages. The first stage is a preprocessing step that involves the construction of a tree, while the second stage performs actual filtering using this tree. The third stage is reconstruction, which we have replaced by a visualization step. Building the tree takes several seconds for small volumes, and in the order of minutes for larger volumes.

We have proposed several extensions to the Max-Tree data structure that allow efficient visualization. Direct volume rendering based on splatting has turned out to be a viable approach when the data are sparse. For more dense data, a better performance is obtained by performing the rendering on graphics hardware. For this purpose, we have introduced a method to represent the Max-Tree as a lookup table on the graphics hardware. Then, filtering only requires an update of this lookup table, which is much faster than a traditional approach of volume reconstruction and subsequent transfer to the graphics hardware. We have also introduced extensions that

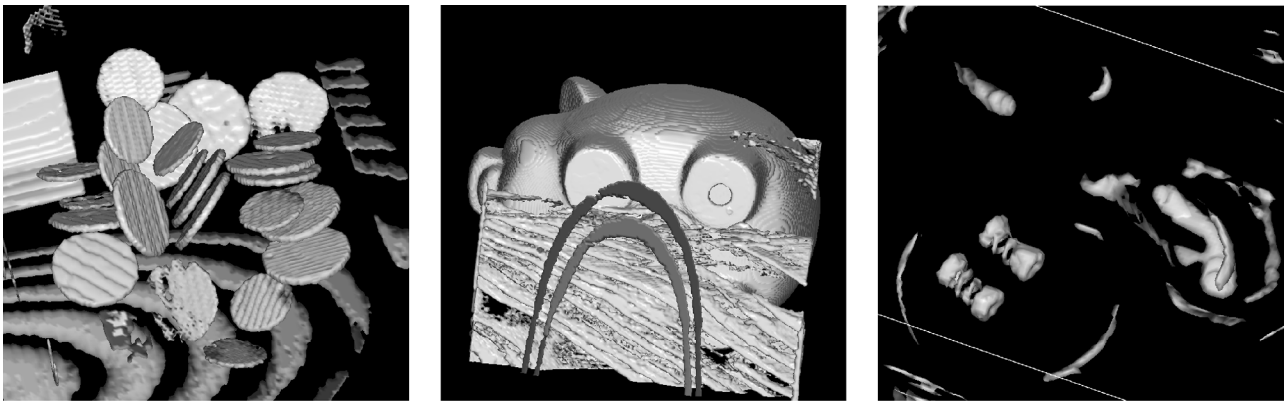

(a) (b) (c)

Fig. 7. Piggy bank filtering results for various attributes. (a) Flatness attribute reveals the coins (filter threshold $\lambda = 100.0$, isolevel threshold $t = 20$). (b) Base of the piggy bank is made of wood, as the sparseness attribute shows ($\lambda = 6.5, t = 10$). (c) Elongation attribute makes the two springs inside a plug in the belly of the piggy bank visible ($\lambda = 5.0, t = 150$).

allow fast isolevel queries in the Max-Tree data structure. The performance comes close to the performance of the interval tree; however, our method has the advantage that both filter threshold browsing and isolevel browsing are fast. The interval tree cannot be used for both these purposes, since it requires a large amount of preprocessing time to construct the tree.

In the current comparison, the MTNN and MTTL methods come out best, but their drawback is that they require the entire label volume T_v to be stored on the graphics card. This means that very large volumes cannot be visualized in this way. Both splatting and isosurfacing are feasible if graphics memory is insufficient, though splatting only works at adequate speeds if the volume is sparse, and isosurfacing is also only possible at interactive rates if the active cell count is low. For angiographic datasets, sparse volumes are obtained by filter threshold settings near the optimum.

In principle, both MTNN and MTTL could be extended to other connected filters, such as the autodual filters of Monasse and Guichard [23], or the even more general method of Soille [46]. This is because any connected filter only ever merges flat zones, or assigns new grey levels to them [47]. Thus, any connected filter can be constructed by first labelling all flat zones in a volume, computing a lookup table containing new grey levels for every flat zone, and computing the new volume by simple table lookup. If recomputing the lookup table can be done efficiently, it is possible to use a variant of MTNN or MTTL for rapid visualization.

The attributes stored for each voxel in the Max-Tree could be used in many different ways other than filtering. In particular, modifying color and opacity would be interesting ways to manipulate the visual representation of these volumes. As the Max-Tree provides a decomposition in connected components, a classification scheme could assign each of the components a different color, texture, or annotation. The speed of recomputation of these attributes, even if fairly complicated moment invariants are used, means such interaction can readily include changing the attributes themselves, rather than just changing visualization parameters such as transfer-function settings or iso-surface levels.

It might also be possible to perform progressive refinement based on the component structure stored in the Max-Tree, rendering the most important components first, and gradually adding less important ones. Unlike other progressive refinement methods, the shape preserving nature of connected filters would mean that the rendered components would appear at full resolution, rather than as a blurred version first [35], [43].

REFERENCES

[1] U. Braga-Neto and J. Goutsias, "Grayscale level connectivity: Theory and applications," *IEEE Trans. Image Process.*, vol. 13, no. 12, pp. 1567–1580, Dec. 2004.

[2] U. Braga-Neto and J. Goutsias, "Object-based image analysis using multiscale connectivity," *IEEE Trans. Pattern Anal. Mach. Intell.*, vol. 27, no. 6, pp. 892–907, Jun. 2005.

[3] R. Jones, "Connected filtering and segmentation using component trees," *Comput. Vis. Image Understand.*, vol. 75, pp. 215–228, 1999.

[4] V. Metzler, T. Aach, and C. Ties, "A novel object-oriented approach to image analysis and retrieval," in *Proc. 5th IEEE Southwest Symp. Image Anal. Interpret.*, 2002, pp. 14–18.

[5] G. K. Ouzounis and M. H. F. Wilkinson, "Mask-based second generation connectivity and attribute filters," *IEEE Trans. Pattern Anal. Mach. Intell.*, vol. 29, no. 2, pp. 990–1004, Feb. 2007.

[6] G. K. Ouzounis and M. H. F. Wilkinson, "Filament enhancement by non-linear volumetric filtering using clustering-based connectivity," in *Proc. Int. Workshop Intell. Comput. Pattern Anal. Synth.*, N. Zheng, X. Jiang, and X. Lan, Eds., Xi'an, China, 2006, vol. 4153, pp. 317–327.

[7] A. Sofou, C. Tzafestas, and P. Maragos, "Segmentation of soilsection images using connected operators," in *Proc. Int. Conf. Image Processing*, 2001, pp. 1087–1090.

[8] C. S. Tzafestas and P. Maragos, "Shape connectivity: Multiscale analysis and application to generalized granulometries," *J. Math. Imag. Vis.*, vol. 17, pp. 109–129, 2002.

[9] F. Cheng and A. N. Venetsanopoulos, "An adaptive morphological filter for image processing," *IEEE Trans. Image Process.*, vol. 1, no. 1, pp. 533–539, Oct. 1992.

[10] E. J. Breen and R. Jones, "Attribute openings, thinnings and granulometries," *Comput. Vis. Image Understand.*, vol. 64, no. 3, pp. 377–389, 1996.

[11] E. R. Urbach and M. H. F. Wilkinson, "Shape-only granulometries and grey-scale shape filters," in *Proc. Int. Symp. Mathematical Morphology*, 2002, pp. 305–314.

[12] E. R. Urbach, J. B. T. M. Roerdink, and M. H. F. Wilkinson, "Connected shape-size pattern spectra for rotation and scale-invariant classification of gray-scale images," *IEEE Trans. Pattern Anal. Mach. Intell.*, vol. 29, no. 2, pp. 272–285, Feb. 2007.

[13] M. H. F. Wilkinson and M. A. Westenberg, "Shape preserving filament enhancement filtering," in *Proc. MICCAI*, W. J. Niessen and M. A. Viergever, Eds., 2001, vol. 2208, pp. 770–777.

[14] P. Salembier, A. Oliveras, and L. Garrido, "Anti-extensive connected operators for image and sequence processing," *IEEE Trans. Image Process.*, vol. 7, no. 4, pp. 555–570, Apr. 1998.

[15] A. Meijster, M. A. Westenberg, and M. H. F. Wilkinson, "Interactive shape preserving filtering and visualization of volumetric data," in *Proc. 4th IASTED Conf. Comp. Signal Image Processing*, Kauai, HI, Aug. 12–14, 2002, pp. 640–643.
[16] L. A. Westover, "Footprint evaluation for volume rendering," *Comput. Graph.*, vol. 24, no. 4, pp. 367–376, 1990.
[17] B. Cabral, N. Cam, and J. Foran, "Accelerated volume rendering and tomographic reconstruction using texture mapping hardware," in *Proc. Workshop on Volume Visualization*, Washington, DC, Oct. 1994, pp. 91–98.
[18] S. Morse, "Concepts of use in computer map processing," *Commun. ACM*, vol. 12, pp. 147–152, 1969.
[19] J. Roubal and T. K. Peucker, "Automated contour labeling and the contour tree," in *Proc. AUTO-CARTO 7*, 1985, pp. 472–481.
[20] M. J. van Kreveld, R. W. van Oostrum, C. Bajaj, V. Pascucci, and D. Schikore, "Contour trees and small seed sets for isosurface traversal," in *Proc. 13th Annu. ACM Symp. Computational Geometry*, New York, pp. 212–220.
[21] H. Carr, J. Snoeyink, and U. Axen, "Computing contour trees in all dimensions," *Computat. Geom.*, vol. 24, pp. 75–94, 2003.
[22] V. Pascucci and K. Cole-McLaughlin, "Efficient computation of the topology of level sets," in *Proc. IEEE Visualization*, Boston, MA, 2002, pp. 187–194.
[23] P. Monasse and F. Guichard, "Fast computation of a contrast invariant image representation," *IEEE Trans. Image Process.*, vol. 9, no. 5, pp. 860–872, May 2000.
[24] L. Najman and M. Couprie, "Building the component tree in quasi-linear time," *IEEE Trans. Image Process.*, vol. 15, no. 11, pp. 3531–3539, Nov. 2006.
[25] C. Berger, T. Géraud, R. Levillain, and N. Widynski, "Effective component tree computation with application to pattern recognition in astronomical imaging," presented at the IEEE Int. Conf. Image Processing, San Antonio, TX, Sep. 2007.
[26] T. T. Elvins, "A survey of algorithms for volume visualization," *Comput. Graph.*, vol. 26, no. 3, pp. 194–201, 1992.
[27] W. E. Lorensen and H. E. Cline, "Marching cubes: A high resolution 3D surface construction algorithm," *Comput. Graph.*, vol. 21, no. 4, pp. 163–169, 1987.
[28] M. Levoy, "Display of surfaces from volume data," *IEEE Comput. Graph. Appl.*, vol. 8, no. 3, pp. 29–37, Mar. 1988.
[29] C. R. Johnson and C. D. Hansen, Eds., *The Visualization Handbook*. Burlington, MA: Elsevier Butterworth-Heinemann, 2005.
[30] P. Cignoni, P. Marino, C. Montani, E. Puppo, and R. Scopigno, "Speeding up isosurface extraction using interval trees," *IEEE Trans. Vis. Comput. Graph.*, vol. 3, no. 2, pp. 158–170, Feb. 1997.
[31] T. Itoh, Y. Yamaguchi, and K. Koyamada, "Fast isosurface generation using the volume thinning algorithm," *IEEE Trans. Vis. Comput. Graph.*, vol. 7, no. 1, pp. 32–46, Jan. 2001.
[32] H. Carr and J. Snoeyink, "Path seeds and flexible isosurfaces using topology for exploratory visualization," in *Proc. Joint Eurographics—IEEE TVCG Symp. Visualization*, 2003, pp. 49–58.
[33] D. Laur and P. Hanrahan, "Hierarchical splatting: A progressive refinement algorithm for volume rendering," *Comput. Graph.*, vol. 25, no. 4, pp. 285–288, 1991.
[34] M. H. Gross, L. Lippert, R. Dittrich, and S. Häring, "Two methods for wavelet-based volume rendering," *Comput. Graph.*, vol. 21, no. 2, pp. 237–252, 1997.
[35] M. A. Westenberg and J. B. T. M. Roerdink, "X-ray volume rendering through two-stage splatting," *Mach. Graph. Vis.*, vol. 9, no. 1/2, pp. 307–314, 2000.
[36] T. Malzbender, "Fourier volume rendering," *ACM Trans. Graph.*, vol. 12, no. 3, pp. 233–250, 1993.
[37] M. A. Westenberg and J. B. T. M. Roerdink, "Frequency domain volume rendering by the wavelet X-ray transform," *IEEE Trans. Image Process.*, vol. 9, no. 7, pp. 1249–1261, Jul. 2000.
[38] H. Pfister, J. Hardenbergh, J. Knittel, H. Lauer, and L. Seiler, "The VolumePro real-time ray-casting system," in *Proc. Siggraph*, Los Angeles, CA, Aug. 1999, pp. 251–260.
[39] F. Dachille, K. Kreeger, B. Chen, I. Bitter, and A. Kaufman, "High-quality volume rendering using texture mapping hardware," in *Proc. Eurographics/SIGGRAPH Workshop on Graphics Hardware*, 1998, pp. 69–76.
[40] M. K. Hu, "Visual pattern recognition by moment invariants," *IRE Trans. Inf. Theory*, vol. IT-8, pp. 179–187, 1962.
[41] F. A. Sadjadi and E. L. Hall, "Three dimensional moment invariants," *IEEE Trans. Pattern Anal. Mach. Intell.*, vol. PAMI-2, pp. 127–136, 1980.
[42] C.-H. Lo and H.-S. Don, "3-D moment forms: Their construction and application to object identification and positioning," *IEEE Trans. Pattern Anal. Mach. Intell.*, vol. PAMI-11, pp. 1053–1064, 1989.
[43] J. B. T. M. Roerdink, "Multiresolution maximum intensity volume rendering by morphological adjunction pyramids," *IEEE Trans. Image Process.*, vol. 12, no. 6, pp. 653–660, Jun. 2003.
[44] W. Cai and G. Sakas, "Maximum intensity projection using splatting in sheared object space," in *Proc. Eurographics*, 1998, vol. 17, no. 3, pp. C113–C124.
[45] H. J. A. M. Heijmans, *Morphological Image Operators*. Boston, MA: Academics, 1994.
[46] P. Soille, "Beyond self-duality in morphological image analysis," *Image Vis. Comput.*, vol. 23, pp. 249–257, 2005.
[47] P. Salembier and J. Serra, "Flat zones filtering, connected operators, and filters by reconstruction," *IEEE Trans. Image Process.*, vol. 4, no. 8, pp. 1153–1160, Aug. 1995.

Michel A. Westenberg received the M.Sc. degree in computing science and the Ph.D. degree in mathematics and natural sciences from the University of Groningen (RUG), Groningen, The Netherlands, in 1996 and 2001, respectively.

From 2001 to 2004, he was a Postdoctorate with the Institute for Mathematics and Computing Science, RUG. From 2004 to 2005, he was a Humboldt Research Fellow at the Institute for Visualization and Interactive Systems, University of Stuttgart, Germany, and was funded by the Alexander von Humboldt Foundation (Germany). Currently, he is a Postdoctorate with the Institute for Mathematics and Computing Science (RUG), where he works on visualization methods in bioinformatics.

Jos B. T. M. Roerdink (SM'03) received the M.Sc. degree in theoretical physics from the University of Nijmegen, The Netherlands, in 1979, and the Ph.D. degree from the University of Utrecht, The Netherlands, in 1983.

Following his Ph.D. degree and a two-year position (1983 to 1985) as a Postdoctoral Fellow at the University of California, San Diego, both in the area of stochastic processes, he joined the Centre for Mathematics and Computer Science, Amsterdam, The Netherlands, where he worked from 1986 to 1992 on image processing and tomographic reconstruction. He was appointed to Associate Professor (1992) and Full Professor (2003), respectively, at the Institute for Mathematics and Computing Science of the University of Groningen, Groningen, The Netherlands, where he currently holds a Chair in Scientific Visualization and Computer Graphics. His current research interests include biomedical visualization, neuroimaging, and bioinformatics.

Michael Wilkinson (SM'06) received the M.Sc. degree in astronomy from the Kapteyn Laboratory, University of Groningen (RUG), Groningen, The Netherlands, in 1993, and the Ph.D. degree from the Institute of Mathematics and Computing Science (IWI), RUG in 1995.

He worked on image analysis of intestinal bacteria at the Department of Medical Microbiology, RUG. This work formed the basis of his Ph.D. work at the IWI, RUG. He was appointed as Researcher at the Centre for High Performance Computing, RUG, where he worked on biomedical simulations on parallel computers. During that time, he edited the book *Digital Image Analysis of Microbes* (Wiley, 1998) together with F. Schut. After this, he was a Researcher at the IWI on image analysis of diatoms. He is currently a Lecturer at the IWI, working on mathematical morphology and computer simulation in biomedical contexts.